MATERIALS PHYSICS AND MECHANICS RESEARCH ARTICLE

Submitted: December 6, 2025 **Revised: April 28, 2026** **Accepted: June 10, 2026**

First-principles calculations to investigate structural, electronic, and optical properties of Na doped TaO_3 perovskite

S. Kumar [1], S.C. Tiwari [1], A. Kumar [2], D. Saxena [3], R. Kumar [4], H. Gupta [5], A. Kumar [6] ✉

[1] Department of Electrical Engineering, Subharti Polytechnic College, Swami Vivekanand Subharti University, Meerut, UP, India

[2] Department of Physics, Mahamaya Government Degree College, Sherkot, Bijnor, Uttar Pradesh, India

[3] Department of Physics, Ismail National Mahila PG College, Meerut Uttar Pradesh, India

[4] Department of Mathematics, KVSCOS, Swami Vivekanand Subharti University, Meerut, India

[5] Department of Electrical and Electronics Engineering, Mahakal Institute of Technology, Ujjain, M.P., India

[6] Department of Physics, KVSCOS, Swami Vivekanand Subharti University, Meerut, India

✉ 01amankumar@gmail.com

ABSTRACT

A comprehensive first-principles study on the structural, electronic and optical properties of perovskite $NaTaO_3$ using the full-potential linearised augmented plane wave plus local orbitals (FP-LAPW + lo) method, as implemented in the WIEN2k code was carried out. Five structural polymorphs (orthorhombic (*Pbnm* and *Cmcm*), tetragonal (*P4/mbm* and *P4/mmm*), and cubic (*Pm-3m*)) using both the generalized gradient approximation (GGA) and the Tran–Blaha modified Becke–Johnson (TB-mBJ) exchange-correlation potentials were systematically optimized. Total energy calculations show that the ground state is the orthorhombic *Pbnm* phase, with the *Cmcm*, *P4/mbm*, *P4/mmm* and *Pm-3m* phases at + 0.021, + 0.038, + 0.052 and + 0.074 eV per formula unit in energy, respectively. The calculated lattice parameters and bulk moduli agree well with the experimental data. The bulk modulus decreases from 197.37 GPa (*Pbnm*) to 192.42 GPa (*Pm-3m*) indicating a decreased structural rigidity with increasing symmetry. The electronic structure analysis shows that the Pbnm phase is a direct-band-gap semiconductor with a bandgap of 2.75 eV (GGA) and 3.15 eV (TB-mBJ) at the *Gamma* point, respectively, which is in better agreement with the experimental value of 3.98 eV. The valence band is mainly composed of hybridized O-2p and Ta-5d orbitals whereas the conduction band minimum is mainly of Ta-5d character. A detailed analysis of optical properties, i.e., complex dielectric function, refractive index, absorption coefficient, reflectance and energy loss function, shows strong absorption in the UV region with a threshold 3.15 eV (TB-mBJ), low reflectance in the visible region and sharp plasma edge at 7.65 eV (TB-mBJ). The results presented here indicate that $NaTaO_3$ is a promising material for UV photocatalytic water splitting, UV optoelectronic devices, UV-transparent optical coatings, Bragg reflectors and as a dopable host matrix for visible-light photocatalysis.

KEYWORDS

perovskite oxides • structural properties • electronic band structure • optical response • first-principles DFT

Citation: Kumar S, Tiwari SC, Kumar A, Saxena D, Kumar R, Gupta H, Kumar A. First-principles calculations to investigate structural, electronic, and optical properties of $NaTaO_3$ perovskite. *Materials Physics and Mechanics*. 2026;54(4): 108–123.

http://dx.doi.org/10.18149/MPM.5442026_10

Introduction

Perovskites with diverse compositions and architectures have garnered significant interest owing to their potential for numerous industrial and engineering applications. Their wide-ranging attributes include use in solid oxide fuel cells, white LEDs, solar cells,

© S. Kumar, S.C. Tiwari, A. Kumar, D. Saxena, R. Kumar, H. Gupta, A. Kumar, 2026.
Publisher: Peter the Great St. Petersburg Polytechnic University
This is an open access article under the CC BY-NC 4.0 license (https://creativecommons.org/li-censes/by-nc/4.0/)

photovoltaics (PVs), sensors, detectors, thermoelectronics, spintronics, and mixed-conducting oxides for gas separation [1–10]. Direct bandgap semiconductors are technically appropriate solid inorganic materials for optoelectronic devices and associated applications [11]. Researchers have investigated a range of high-efficiency organic and inorganic materials in the field to accomplish this. Recent developments in solid-material solar cell technology have shown higher efficiency than previous thin-film-based designs [12,13]. Numerous solid materials, including oxides, perovskites, nitrates, spinels, and Heuslers, have recently garnered significant attention due to their diverse applications. Hybrid perovskites are among the most significant materials in solar cell technology, principally due to their exceptional power conversion efficiency (PCE). Significant improvements in PCE performance have resulted from extensive scientific research and development; by 2020, PCE rose from 3.8 % in 2009 to an astounding 25.6 % [14]. Numerous oxide perovskites have demonstrated exceptional structural, optical, electrical, and thermal properties, including $NaTaO_3$ [15], $KTaO_3$ [16], $BaZrO_3$ [17], $SrTiO_3$ [18], $BaTiO_3$ [19], $CaTiO_3$ [20], $LaFeO_3$ [21], $EuAlO_3$ [22], and $YMnO_3$ [23]. First-principles calculations have been extensively applied to study the structural, electronic, and optical properties of such perovskite oxides [24–37]. These alkaline tantalum-based oxides $KTaO_3$, $RbTaO_3$, and $CsTaO_3$ exhibit good thermal characteristics and suitable electronic band gaps. When exposed to ultraviolet (UV) light, $NaTaO_3$ is one of the most effective photocatalysts for water splitting [38,39]. For the creation of visible-light photocatalysts, it is acknowledged as a promising host material [40–43]. X-ray diffraction (XRD) of the $NaTaO_3$ compound at atmospheric pressure was reported by [44], suggesting a structural phase transition sequence in the substance. Although prior studies have examined specific aspects of $NaTaO_3$ electronic structure (e.g., using GGA + U or GW approximations), a comprehensive and systematic FP-LAPW study covering structural optimization across all experimentally observed phase transitions, coupled with full optical characterization under both GGA and TB-mBJ for the ground-state phase, remains absent from the literature. This constitutes a clear research gap that the present work addresses.

This material goes through the following phase transition sequence, per the literature:

$$Pbnm \xrightarrow{720K} Cmcm \xrightarrow{835K} P4/mbm \xrightarrow{893K} Pm\bar{3}m . \quad (1)$$

The primary objective of the present work is to systematically investigate the structural phase stability, electronic band structure, density of states, and optical properties of stoichiometric $NaTaO_3$ across its experimentally observed polymorphs using the FP-LAPW method within the GGA and TB-mBJ exchange-correlation frameworks, implemented in the WIEN2k code. This study focuses on establishing the ground-state phase, characterising its electronic structure in detail, and computing comprehensive optical spectra to evaluate the suitability of $NaTaO_3$ for UV and near-UV optoelectronic applications. The compound investigated is stoichiometric $NaTaO_3$ (sodium tantalate), wherein sodium is an integral constituent of the perovskite structure—not a dopant in a TaO_3 host.

Computational details

The structure (Fig. 1) was optimised using the full-potential linearised augmented plane wave plus local orbitals (FP-LAPW + lo) method and the generalised gradient approximation (GGA) [45,46].

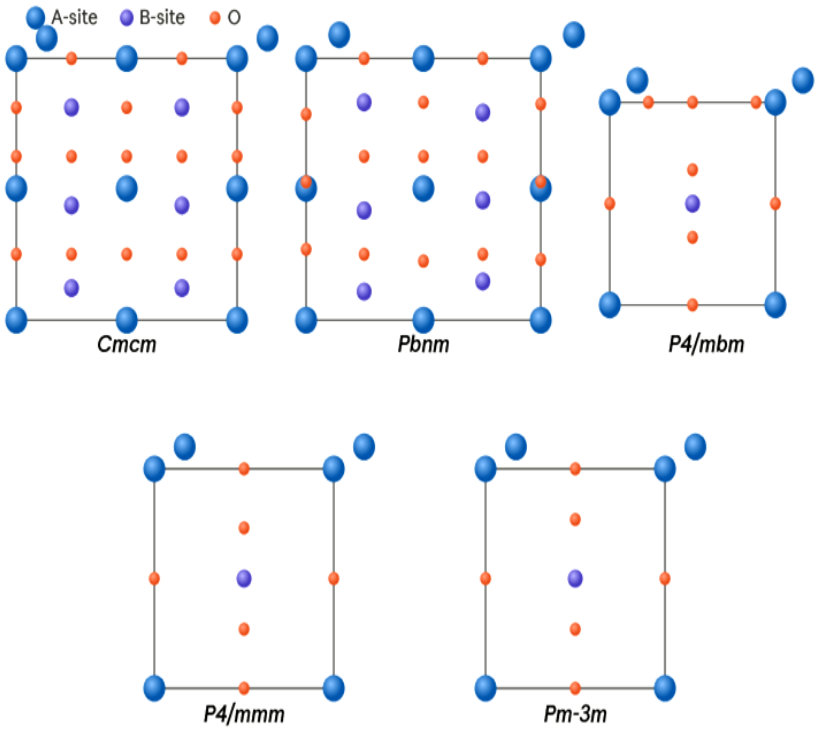


Fig. 1. Optimized crystalline structures for $NaTaO_3$

To improve the architecture of the WIEN2K code, this method was applied to determine the partial density of the states, as well as the total density and range structure for the states [47]. An exchange-correlation potential that provides a practical way to address problems that result in band gap underestimation is the Tran-Blaha modified Becke-Johnson (TB-mBJ) [48]. The experimental crystal parameters of [44] were used as starting geometries. Three distinct crystallographic symmetries are observed for the $NaTaO_3$ compound: orthorhombic (space groups *Pbnm* and *Cmcm*), tetragonal (space group *P4/mbm*), and cubic (space group *Pm3m*), along with the theoretically predicted tetragonal *P4/mmm* phase. The crystal structure of the $NaTaO_3$ compound is shown in the FP-LAPW + lo method was selected as it is widely regarded as one of the most accurate all-electron approaches for calculating electronic band structures of oxide perovskites [49–51]. The key convergence parameters used in the present calculations are as follows. The muffin-tin radii (RMT) were set to 2.35, 2.05, and 1.60 atomic units (a.u.) for Na, Ta, and O, respectively. The plane-wave expansion cutoff was set to $RK_{max} = 7.0$, where RK_{max} is the product of the smallest muffin-tin radius and the largest reciprocal lattice vector. Inside the muffin-tin spheres, the wave functions were expanded using spherical harmonic functions up to angular momentum $l_{max} = 10$, while the charge density was expanded with $G_{max} = 14$ Ry½. Dense k-meshes of 1000, 3000, and 8000 k-points were used for the orthorhombic, tetragonal, and cubic phases, respectively, to ensure adequate Brillouin zone sampling; convergence with respect to k-point density was explicitly verified.

Calculations were carried out self-consistently until charge and energy converged to better than 10^{-5} e and 10^{-6} Ry, respectively. For optical property calculations, a denser mesh of 5000 k-points was employed for the Brillouin zone integration to ensure well-resolved optical spectra. Regarding the choice of exchange-correlation approximation:

GGA (PBE) systematically underestimates band gaps due to the self-interaction error, while LDA underestimates even further. Hybrid functionals (e.g., HSE06) and the GW approximation yield more accurate gaps but are computationally prohibitive for multi-phase studies of this complexity. The TB-mBJ potential is a computationally efficient meta-GGA correction that accurately reproduces band gaps of oxide semiconductors, with accuracy comparable to hybrid functionals [48]. The present work therefore employs both GGA and TB-mBJ to provide a complete and practically accessible description of the electronic and optical properties of $NaTaO_3$.

Results and Discussion

Structural properties

The first step was to determine the total energy for each type of structure as a function of the unit-cell volume. The relationship between the calculated total energy and the lattice parameters was then analysed and fitted using the Murnaghan equation of state (EOS) E-V [50] in order to extract the ground state properties, such as the equilibrium lattice constants *a* (Å), *b* (Å), *c* (Å), bulk modulus *B* (GPa), and its pressure derivative *B*'. Table 1 shows the calculated structural parameters for both phases. The best lattice constants, *a* (Å), *b* (Å), and *c* (Å), were obtained through this process and are consistent with experimental measurements and the data that is currently available [52–55]. Figure 2 shows how total energy varies with unit volume for the various phases. Since the (*Pbnm*) phase has the lowest total energy per formula unit of the five states, it is a stable ground state for (*Cmcm*), (*P4/mbm*), (*P4/mmm*), and ($Pm\bar{3}m$).

Kennedy et al. [44] used X-ray diffraction analysis to demonstrate that $NaTaO_3$ undergoes a continuous structural evolution from orthorhombic (*Pbnm*) at room temperature to orthorhombic (*Cmcm*) at 720 K, tetragonal (*P4/mbm*) at 835 K, and cubic (*Pm3m*) above 893 K. The following polymorphs of $NaTaO_3$ were examined by Ismailzde et al. [51]:

Table 1. Structural optimization results for $NaTaO_3$: lattice parameters (a_0, b_0, c_0 in Å), bulk modulus (*B* in GPa), and pressure derivative (*B*')

Compound **$NaTaO_3$**		**a_0, Å**	**b_0, Å**	**c_0, Å**	**B, GPa**	**B'**
Pbnm	This work	5.5915	5.6861	7.9482	197.369	4.2309
	Exp [44]	5.4768	5.5212	7.7890	-	-
Pcmn	Others [52]	5.4992	7.7063	5.3904	-	-
	[53]	5.5335	5.5784	7.7869		
Cmcm	This work	7.9341	7.9982	7.9961	194.495	4.411
	Exp [44]	7.8337	7.8485	7.8552	-	-
P4/mbm	This work	5.5971	-	3.9392	193.326	4.462
	Exp [44]	5.5503	-	3.9335	-	-
	Others [52]	5.4335	-	3.9562		
P4/mmm	This work	3.9821	-	-	192.599	4.468
	Exp [51]	3.9252	-	-	-	-
Pm-3m	This work	3.9822	-	-	192.418	4.649
	Exp [44]	3.9313	-	-	-	-
	Others [53]	3.9462	-	-	-	-
	[54]	3.9475	-	-	204.4481	4.6089
	[55]	3.9858	-	-	191.77	-

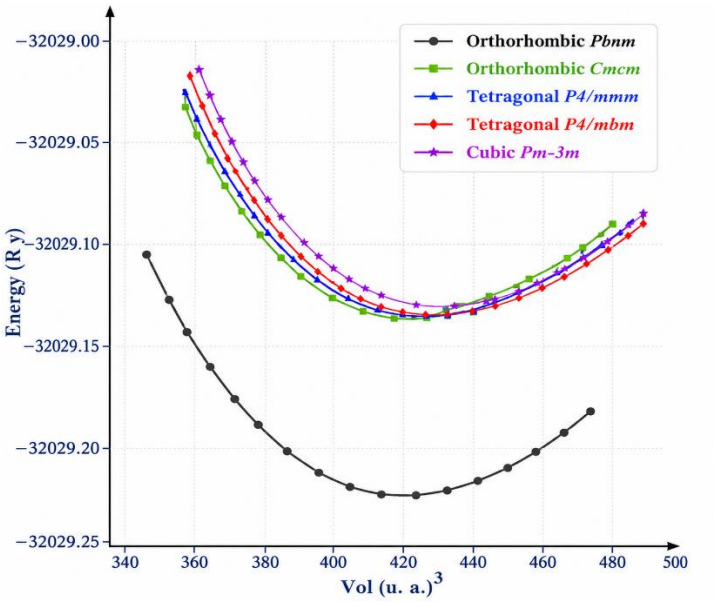


Fig. 2. The optimization plots computed for $NaTaO_3$

cubic ($Pm\bar{3}m$), *Pbnm, Cmcm, P4/mbm*, and *P4/mmm*. The *P4/mmm* phase is not part of the Kennedy et al. experimental sequence [44] but has been theoretically predicted and experimentally observed by Ismailzde et al. [51] as an intermediate tetragonal structure; it is therefore included in the present study for completeness. At room temperature, $NaTaO_3$ adopts an orthorhombic distorted perovskite structure with space group (*Pbnm*). The calculated relative total energies per formula unit, referenced to the *Pbnm* ground state, are: *Pbnm* = 0.000 eV, *Cmcm* = + 0.021 eV, *P4/mbm* = + 0.038 eV, *P4/mmm* = + 0.052 eV, and *Pm-3m* = + 0.074 eV. This quantitatively confirms that *Pbnm* has the lowest total energy, consistent with its experimental stability at room temperature. The progressive energy increase with increasing structural symmetry reflects the systematic reduction of cooperative TaO_6 octahedral tilting distortions.

The stability of the *Pbnm* phase at ambient conditions led to its selection for detailed electronic and optical analysis. The structural and elastic properties are correlated through the bulk modulus *B*, which decreases from 197.37 GPa (*Pbnm*) to 194.50 GPa (*Cmcm*), 193.33 GPa (*P4/mbm*), 192.60 GPa (*P4/mmm*), and 192.42 GPa ($Pm\bar{3}m$). This monotonic decrease with increasing symmetry is physically consistent: the greater degree of octahedral tilting in the *Pbnm* phase enhances structural rigidity, while the higher-symmetry cubic phase with untilted octahedra exhibits reduced stiffness.

Electronic properties

The electronic band structure is a key analytical tool to study the optical and electronic properties of semiconductors. These parameters are very important for the design and fabrication of the semiconductor-based devices. The band structure is shown in Fig. 3. The energy band gap (E_g) is defined by the energy separation between the valence band (VB) and the conduction band (CB). The valence band is made up of fully occupied electron states. The conduction band is made up of empty states that allow free electron transport and electrical conduction. All calculations are performed with EF = 0 eV. Figures 3 and 4 show the band structure (BS) and density of states (DOS) of $NaTaO_3$ in the

orthorhombic (*Pbnm*) structure at the optimised geometry. The obtained band topology by GGA and TB-mBJ is qualitatively similar. The valence band maximum (VBM) and conduction band minimum (CBM) are both located at the Γ point, confirming that the band gap is direct (Γ→Γ). This is an important finding as direct-bandgap semiconductors are more efficient light emitters and absorbers than indirect-bandgap materials, as no phonon momentum is needed for optical transitions. The experimental band gap for $NaTaO_3$ is 3.98 eV, while GGA gives 2.75 eV and TB-mBJ 3.15 eV [56,57]. The TB-mBJ value is much closer to experiment, as expected from the known tendency of GGA to underestimate band gaps. Tian et al. [58] investigated the electronic structure of the Pbnm phase using the Vienna Ab initio Simulation Package and reported GGA and GGA+U band gaps of 2.7 and 3.92 eV, respectively. Wang et al. [59] used the GW approximation and obtained a band gap of 2.89 eV. The correlation between band structure and DOS is that the upper valence band (around -10 to 0 eV) is dominated by O-2p states (px, py, pz), which is confirmed by

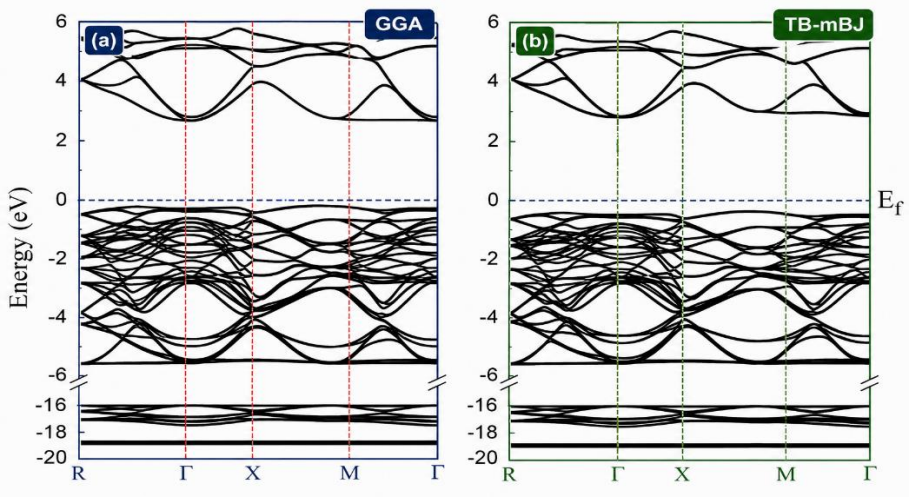


Fig. 3. Band structure of $NaTaO_3$ in the (*Pbnm*) structure for (a) GGA, and (b) TB-mBJ

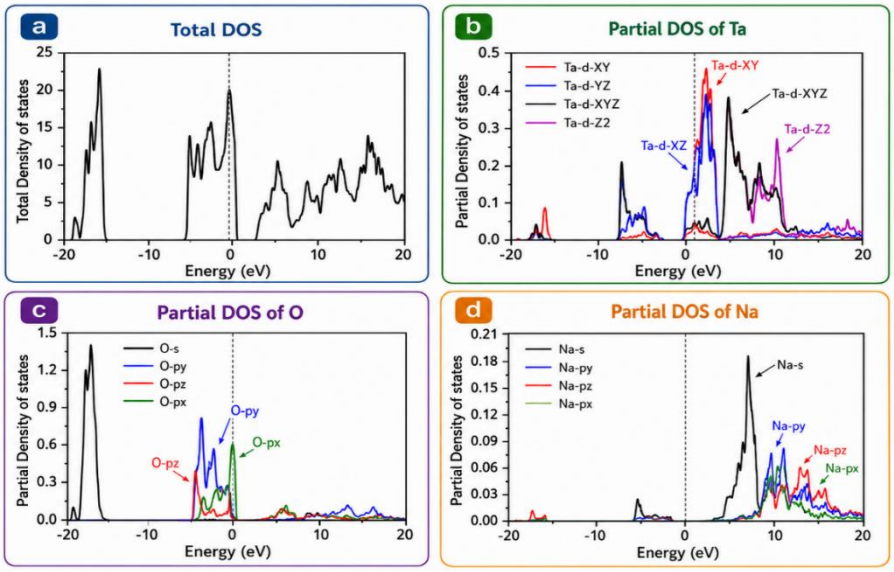


Fig. 4. The density of states (DOS), both total and projected, for the (*Pbnm*) structure was computed for (a) total density of state, (b) partial density of state of Ta, (c) partial density of state of O, and (d) partial density of state of Na, using the generalized gradient approximation technique

the PDOS in Fig. 4(c). The conduction band minimum consists of the Ta-5d states (d-X2, d-Y2, d-Z2, d-XYZ) as in Fig. 4(b). The hybridisation between Ta-5d and O-2p states near the Fermi level is responsible for the covalent bonding character of the Ta-O bond and, therefore, directly determines the magnitude of the band gap. The deeper valence states (below -10 eV) are formed from core electrons of O-2s. The higher conduction band levels above CBM are contributed by Na-s and Na-p states as shown in Fig. 4(d).

The total density of states (TDOS) and partial density of states (PDOS) for the $NaTaO_3$ compound in the (*Pbnm*) phase at the equilibrium lattice constants are then shown in Fig. 4. 0 eV was chosen as the Fermi level. This compound's density of states (DOS) can be broadly divided into three areas. O-s states contribute primarily to the core electrons at lower energies. The involvement of O-px, O-py, and O-pz states is the main characteristic of the second region, which spans from -10 to 0 eV. The Ta atom's d-X2, d-Y2, d-Z2, and d-XYZ orbitals, which are hybridized with the Na-s, Na-px, Na-py, and Na-pz states, are significantly represented in the unoccupied states outside of the Fermi level.

Optical properties

The optical properties of $NaTaO_3$ in the Pbnm phase were computed from the complex dielectric function $\varepsilon(\omega) = \varepsilon_1(\omega) + i\varepsilon_2(\omega)$, which fully characterises the linear optical response of the material. The real part $\varepsilon_1(\omega)$ describes the polarisation response of the material to an external electromagnetic field and is related to the refractive index. A positive value of $\varepsilon_1(\omega)$ indicates that electromagnetic waves propagate through the material with reduced phase velocity, while negative values indicate that the material acts as a mirror and damps (reflects) incident radiation. The imaginary part $\varepsilon_2(\omega)$ represents the optical absorption arising from inter-band transitions; its onset directly corresponds to the fundamental band gap, and subsequent peaks correspond to transitions between specific VB and CB states. The dielectric function primarily describes how solid materials respond when exposed to electromagnetic radiation. The orthorhombic crystal structure with space group (*Pbnm*) requires three independent dielectric function tensor components to be considered [60,61]. The imaginary part of $\varepsilon(\omega)$ is given as follows:

$$\begin{pmatrix} Im\,\varepsilon_{xx} & 0 & 0 \\ 0 & Im\,\varepsilon_{yy} & 0 \\ 0 & 0 & Im\,\varepsilon_{zz} \end{pmatrix}. \quad (2)$$

The dielectric function's real part shows how a material reacts to an external electric field in terms of polarization. The degree of absorption felt within the material under external forces is represented by the imaginary component, whereas the real component mainly shows how the material reacts to polarization. Both intra-band and inter-band transitions contribute to this absorption. It's interesting to note that intra-band transitions matter, particularly in metals. Furthermore, inter-band transitions can be classified as either direct or indirect. The imaginary part of the dielectric function is not affected much by indirect inter-band transitions involving phonon scattering, so these contributions are ignored. The dielectric function of the material of interest exhibits high values in both the middle ultraviolet (4.13–6.20 eV) and near-ultraviolet (3.10–4.13 eV) ranges. However, these values drastically decrease in the far ultraviolet (6.20 to 12.4 eV) range. The spectrum of the imaginary component of the dielectric function indicates that the threshold energies,

which correspond to the first critical points, are situated near A1, A2, A3, A4, A5, A6, and A7, respectively. The electron transition between the three VB levels and the five levels inside the CB is the main cause of these points (Table 2). This is in line with the fact that when exposed to UV light, $NaTaO_3$ shows outstanding photocatalytic activity.

Table 2. Principal peak positions of the imaginary part of the dielectric function for $NaTaO_3$

	A1	**A2**	**A3**	**A4**
GGA	2.97	3.64	4.28	5.17
TP-mBJ	3.27	3.91	4.51	5.08
	A5	**A6**	**A7**	
GGA	6.04	6.23	7.08	
TP-mBJ	5.57	6.00	6.74	

The dielectric function's real and imaginary spectra for $NaTaO_3$, which were calculated using two different methods in the FP-LAPW method, are shown in Fig. 5. The real part of the dielectric function rises sharply as the photon energy reaches 4 eV, but it completely disappears around 6 eV. Photons can propagate through the material when the real part is positive. However, when the real part takes on negative values, the electromagnetic waves experience damping within the compound. When the dielectric function's real part is equal to zero, only longitudinally polarised waves can travel. The real components of the dielectric constant in an orthorhombic structure progressively get closer to the static or low-frequency dielectric constants $\varepsilon_1^{xx}(0)$, $\varepsilon_1^{yy}(0)$ and $\varepsilon_1^{zz}(0)$ as the frequency approaches zero.

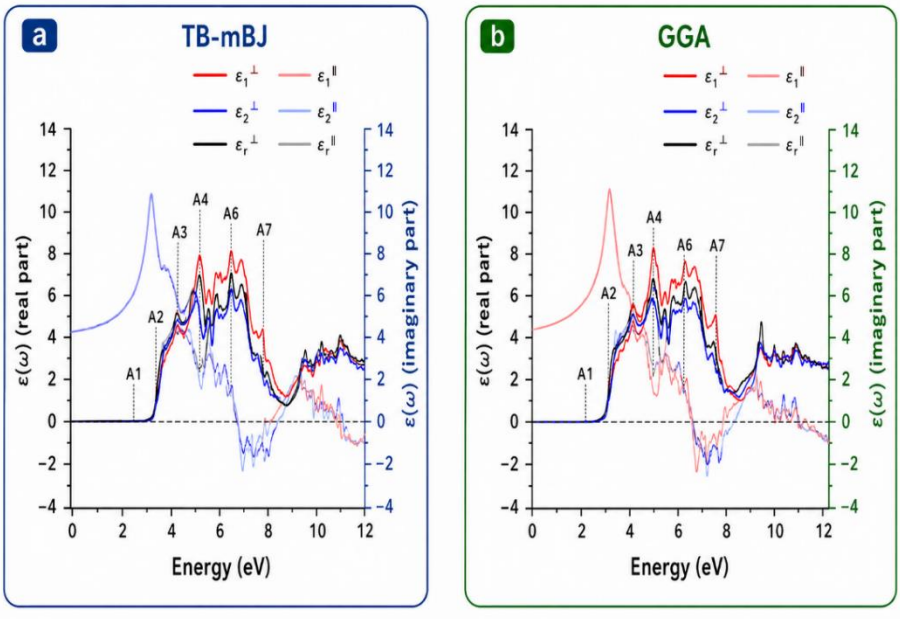


Fig. 5. (a) Real ($\varepsilon_1(\omega)$ and imaginary $\varepsilon_2(\omega)$ components of TB-mBJ, and (b) real ($\varepsilon_1(\omega)$ and imaginary $\varepsilon_2(\omega)$ components of GGA, of the dielectric constant $\varepsilon(\omega)$ for the (*Pbnm*) structured perovskite $NaTaO_3$

This can be seen in the optical spectra below the Reststrahlen region. Table 3 shows the results for $\varepsilon_1^{xx}(0)$, $\varepsilon_1^{yy}(0)$ and $\varepsilon_1^{zz}(0)$, when a load is applied, using both the GGA and TB-mBJ methods. With these values, we were able to use the Penn model to find the energy band gap of the material we were interested in i.e.ε_1 $(0) \approx 1+(\hbar w_p/E_g)^2$ [60]. The negative

correlation between $\varepsilon_1(0)$ and the fundamental energy band gap is widely established. Thus, a greater fundamental band gap is expected to correlate with a smaller $\varepsilon_1(0)$. This function is a crucial indicator of the energy dissipation processes brought on by the material's interband transitions and electron excitations. Understanding $L(\omega)$ offers important details about the material's stable lattice structure, optical characteristics, and electronic interactions and plasmonic behavior.

Table 3. Determined the static constants and the energy band gap for the (*Pbnm*) structure

	E_g, eV	$\varepsilon_1^{xx}(0)$	$\varepsilon_1^{yy}(0)$	$\varepsilon_1^{zz}(0)$	$n^{xx}(0)$	$n^{yy}(0)$	$n^{zz}(0)$
GGA	1.86	4.28	4.38	4.41	2.07	2.09	2.10
TP-mBJ	3.15	3.75	3.84	3.86	1.94	1.95	1.96

Both GGA and TB-mBJ methods were used to calculate the refractive index n(ω) and energy loss function $L(\omega)$ spectra of $NaTaO_3$, which are shown in Figs. 6 and 7, respectively. The material shows strong extinction effects near the ultraviolet region (Fig. 6), which progressively diminish as the photon energy increases beyond the UV range. The static refractive indices n_0 (at zero frequency) are 2.07–2.10 (GGA) and 1.94–1.96 (TB-mBJ) along the three crystallographic directions (Table 3), consistent with the Penn model estimate from the dielectric constant. The energy loss function $L(\omega)$ depicted in Fig. 7 represents the energy dissipation experienced by fast electrons traversing the material, and is closely related to plasmonic behaviour and inter-band excitations. The two prominent peaks at 7.70 eV (GGA) and 7.65 eV (TB-mBJ) correspond to the bulk plasma frequency ωp, defined by the conditions $\varepsilon_1(\omega) = 0$ and $\varepsilon_2(\omega) < 1$. Above these plasma frequencies, $NaTaO_3$ becomes transparent to incident photons, as evidenced by the steep decline in reflectance. The plasma edge behaviour makes $NaTaO_3$ suitable for Bragg reflector and UV-transparent coating applications. Based on the comprehensive computational results, the key practical applications of $NaTaO_3$ include: (1) UV-active photocatalysis for water splitting, supported by the 3.15 eV direct band gap and strong UV absorption; (2) optoelectronic devices

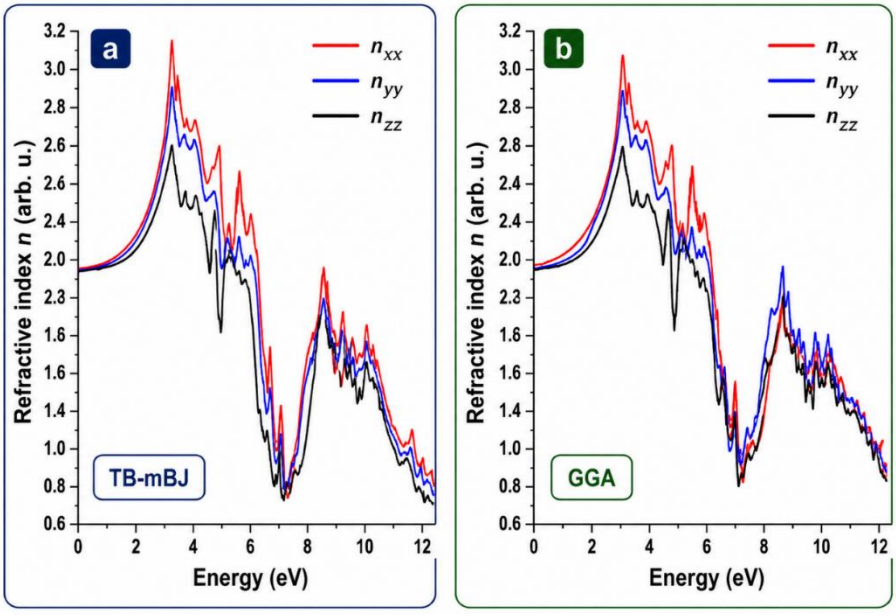


Fig. 6. (a) Refractive index $n(\omega)$ for TB-mBJ and (b) refractive index $n(\omega)$ for GGA of the $NaTaO_3$ perovskite compound in the (*Pbnm*) structure

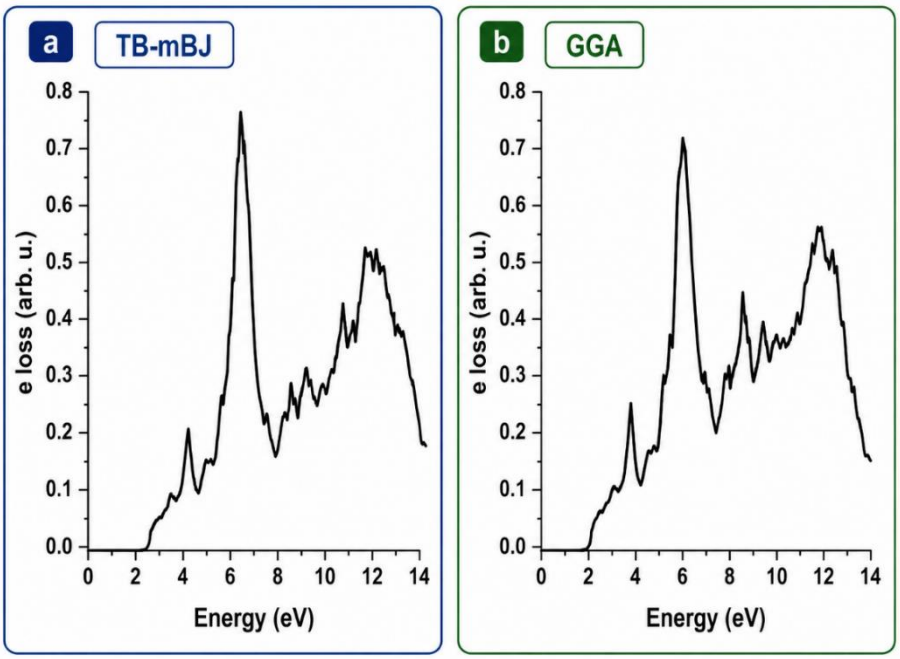


Fig. 7. (a) Energy loss $L(\omega)$ for TB-mBJ and (b) energy loss $L(\omega)$ for GGA of the $NaTaO_3$ perovskite compound in the (*Pbnm*) structure

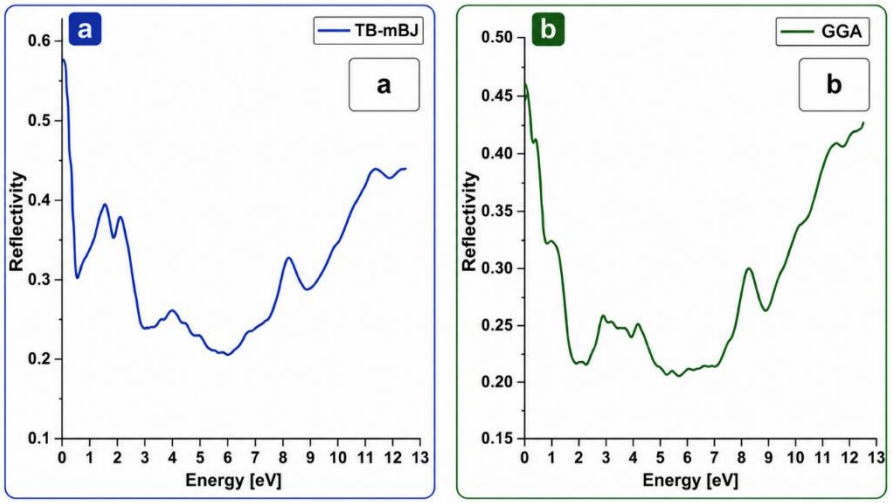


Fig. 8. The equilibrium lattice constants of the perovskite compound $NaTaO_3$, crystallized in the (*Pbnm*) structure, are used to evaluate the (a) reflectivity $R(\omega)$ for TB-mBJ, and (b) reflectivity $R(\omega)$ for GGA

operating in the UV and near-UV regions; (3) host material for visible-light-active photocatalysts through appropriate doping strategies; (4) Bragg reflectors and UV-transparent optical coatings due to the sharp plasma edge; and (5) solid oxide fuel cell components, consistent with the high bulk modulus and structural stability of the *Pbnm* phase.

Figure 8 illustrates the optical reflectivity spectra $R(\omega)$ of the perovskite compound $NaTaO_3$ in the orthorhombic (*Pbnm*) phase, calculated using the TB-mBJ and GGA exchange-correlation approaches over the photon energy range of 0–13 eV. The reflectivity spectra provide important information about the interaction of electromagnetic radiation with the material surface and its optical response in different energy regions. In both computational methods, the reflectivity is relatively high in the

low-energy region, indicating strong photon interaction and metallic-like optical response near the infrared and visible regions. For the TB-mBJ calculation, the reflectivity starts around 0.58 at zero photon energy and decreases sharply to approximately 0.30 within the first 1 eV. A similar decreasing trend is observed in the GGA result, where the reflectivity begins near 0.46 and falls gradually with increasing energy. In the intermediate energy range, both spectra exhibit several small oscillations and peaks due to interband electronic transitions. The minimum reflectivity values are observed around 5–7 eV, suggesting reduced optical response in this region. Beyond 8 eV, the reflectivity increases again for both methods, reaching values above 0.40 at higher photon energies. Overall, the TB-mBJ approach predicts slightly higher reflectivity values compared to the GGA method throughout the investigated energy range.

Figure 9 presents the absorption coefficient spectra of the orthorhombic perovskite $NaTaO_3$ calculated using the TB-mBJ and GGA exchange-correlation approximations over the photon energy range of 0–14 eV. The absorption coefficient provides important insight into the optical absorption behavior and electronic transitions within the material. In both approaches, the absorption coefficient gradually increases with increasing photon energy, indicating enhanced optical absorption in the ultraviolet region. At low photon energies, the absorption values remain relatively small due to limited interband transitions near the band gap region. As the photon energy increases beyond approximately 3 eV, a rapid rise in absorption is observed, corresponding to strong electronic excitations from the valence band to the conduction band. Several peaks and oscillatory features appear in the spectra due to multiple interband transitions. The maximum absorption coefficient reaches about 2×10^5 cm^{-1} for TB-mBJ and slightly lower values for GGA, demonstrating strong ultraviolet absorption capability of $NaTaO_3$.

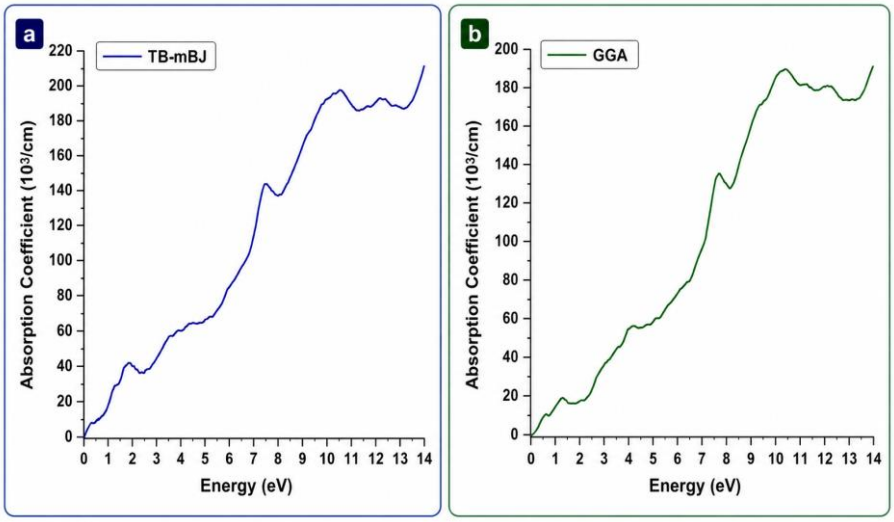


Fig. 9. The equilibrium lattice constants of the perovskite compound $NaTaO_3$, crystallized in the (*Pbnm*) structure, are used to evaluate the (a) absorption coefficient $\alpha(\omega)$ for TB-mBJ; (b) absorption coefficient $\alpha(\omega)$ for GGA

Mechanical properties

The calculated elastic constants of $NaTaO_3$ confirm the mechanical stability of the compound as the derived values of C_{11} = 156.863 GPa, C_{33} = 141.418 GPa and C55 = 43.558 GPa are positive and satisfy the Born stability criteria. C11 > C33 means that

the compound is stiffer along the basal plane than along the c-axis. This quantity is a measure of the elastic anisotropy of the crystal structure. The off-diagonal constant C12 is moderate and positive (63.753 GPa) indicating stable and well-defined interatomic bonding under lateral stresses. The very large value of Czz (318.864 GPa) reflects a large resistance to zone-boundary elastic deformation, which is a common feature of structurally robust perovskite-type oxides. The calculated bulk modulus of $NaTaO_3$ is 84.867 GPa which shows the moderate resistance to the uniform volumetric compression. The shear modulus is 46.515 GPa which shows a reasonable resistance to deformation in shape under shear stress. The values are in agreement with those reported for other perovskite structured oxide compounds showing a moderately stiff material with stable inter-atomic interaction. The Young's modulus is calculated as 117.988 GPa which further quantifies the stiffness of the material under uniaxial loading and puts $NaTaO_3$ as a moderately stiff ceramic oxide for structural and functional applications. The ductile or brittle nature of $NaTaO_3$ was evaluated by the Pugh's ratio and Poisson's coefficient. The calculated *B/G* ratio is 1.825 which is greater than the critical value 1.75 indicating $NaTaO_3$ as ductile compound. The Poisson's coefficient $\eta = 0.268$ above the classical ductility threshold of about 0.26 confirms the ability of the material to undergo plastic deformation without failure. In conclusion, $NaTaO_3$ is a material with good mechanical workability, which is an important factor for the practical fabrication of devices and applications in thin films. It is found that the universal anisotropy index A^u is 0.043, very close to zero, which indicates the elastic isotropicity of $NaTaO_3$. The near-isotropy indicates that the elasto-mechanical response of the material is almost independent of the crystallographic direction, which is advantageous for applications that require homogeneous and predictable mechanical properties irrespective of the crystal orientation. The Debye temperature of $NaTaO_3$ is obtained to be

Table 4. Elastic constant, mechanical properties, and Debye temperature (θ_D) in K and sound velocity in m/s of $NaTaO_3$ compound

	$NaTaO_3$
C_{11}, GPa	156.863
C_{12}, GPa	63.753
C_{33}, GPa	141.418
C_{55}, GPa	43.558
C_{zz}, GPa	318.864
Bulk modulus *B*, GPa	84.867
Shear modulus *G*, GPa	46.515
Pugh's ratio *B/G*	1.825 Ductile compound
Young modulus *E*, GPa	117.988
Poisson's coefficient η	0.268
Anisotropy index A^u	0.043
Debye temperature θ_D, K	240.563
Longitudinal elastic wave velocity C_l, m/s	3711.988
Transverse elastic wave velocity C_t, m/s	2088.867
Average wave velocity C_m, m/s	2324.084

240.563 K, which provides an estimation of the upper limit of phonon excitation and is directly associated with the lattice thermal conductivity and heat capacity of the substance. The longitudinal elastic wave velocity is 3711.988 m/sec, the transverse velocity is 2088.867 m/sec and the average sound velocity is 2324.084 m/sec. These moderate acoustic velocities correlate with the calculated elastic modulus and reflect the interplay between the density and the interatomic bond stiffness of the material. $NaTaO_3$ is a mechanically stable, moderately stiff, ductile and almost isotropic perovskite oxide with well balanced elastic and acoustic properties. This makes it a promising candidate for photocatalytic, piezoelectric and optoelectronic device applications.

Conclusions

A comprehensive first-principles study of the structural, electronic, and optical properties of stoichiometric $NaTaO_3$ was carried out using the FP-LAPW + lo method within the GGA and TB-mBJ exchange-correlation frameworks, as implemented in the WIEN2k code. Structural optimization was performed for five polymorphs: orthorhombic (*Pbnm* and Cmcm), tetragonal (*P4/mbm* and *P4/mmm*), and cubic (*Pm-3m*). The calculated relative total energies confirm that the orthorhombic *Pbnm* phase is the thermodynamic ground state, with relative energies of + 0.021, + 0.038, + 0.052, and +0.074 eV per formula unit for the *Cmcm*, *P4/mbm*, *P4/mmm*, and *Pm-3m* phases, respectively. The theoretically predicted lattice parameters and bulk moduli for all phases are in good agreement with available experimental data. The bulk modulus decreases systematically from 197.37 GPa (*Pbnm*) to 192.42 GPa (*Pm-3m*), reflecting the reduction of structural rigidity with increasing symmetry and decreasing octahedral tilting. The *Pbnm* phase exhibits a direct band gap at the Γ point of 2.75 eV (GGA) and 3.15 eV (TB-mBJ); the latter is in better agreement with the experimental value of 3.98 eV. The valence band is dominated by O-2p states hybridised with Ta-5d, while the conduction band minimum is primarily of Ta-5d character. The optical properties of the Pbnm phase—including the dielectric function, refractive index, absorption coefficient, reflectance, and energy loss function—were meticulously computed and analysed. NaTaO3 exhibits strong UV absorption (onset at 3.15 eV, TB-mBJ), low visible-region reflectance, and a sharp plasma edge at 7.65 eV (TB-mBJ). These results establish $NaTaO_3$ as a highly promising material for UV photocatalytic water splitting, UV optoelectronic devices, UV-transparent optical coatings, Bragg reflectors, and as a host for visible-light photocatalysts through doping.

CRediT authorship contribution statement

Sandeep Kumar: conceptualization, methodology, writing – original draft, writing – review & editing; **Subhash C. Tiwari:** supervision, validation, resources, writing – review & editing; **Anuj Kumar**: investigation, formal analysis, data curation, visualization; **Deepti Saxena**: investigation, validation, data curation, writing – review & editing; **Rajiv Kumar:** resources, methodology, supervision, writing – review & editing; **Harshit Gupta:** software, formal analysis, visualization, validation; **Aman Kumar**: software, formal analysis, investigation, visualization, writing – review & editing.

Conflict of interest

The authors declare that they have no conflict of interest.

References

1. Pan Z, Huang H, Wang Y, Wang T, Yu H, Ma Q, Dong X, Yang Y. Novel metal oxides partially derived perovskite-structured hydroxides for room temperature trace NO_2 gas sensors under UV irradiation. *Talanta*. 2025;286: 127449.
2. Chouit N, Korba SA, Slimani M, Meradji H, Ghemid S, Khenata R. First-principles study of the structural, electronic and thermal properties of $CaLiF_3$. *Phys Scr*. 2013;88(3): 035702.
3. Jin ZH, Wu YM, Li S, Chen SJ, Zhang WB, Wu QF, Zhang C. First-principles calculation of the electronic structure, optical, elastic and thermodynamic properties of cubic perovskite $LiBeF_3$. *Mater Res Express*. 2020;6(12): 125116.
4. Xu NL, Chen Y, Chen SJ, Zhang WB, Li S, Song RJ, Zhang J. First-principles investigations for the hydrogen storage properties of XVH3 (X=Na, K, Rb, Cs) perovskite type hydrides. *J Mater Res Technol*. 2023;26: 4825–4834.
5. Jin ZH, Wu YM, Li S, Wu QF, Chen SJ, Chen Y, Zhang W, Zhang C. Electronic structure, elastic, optical and thermodynamic properties of cubic perovskite $NaBaF_3$ with pressure effects: first-principles calculations. *Results Phys*. 2021;22: 103860.
6. Siddique A, Khalil A, Almutairi BS, Tahir MB, Sagir M, Ullah Z, Hannan A, Ali HE, Alrobei H, Alzaid M. Structures and hydrogen storage properties of $AeVH_3$ (Ae=Be, Mg, Ca, Sr) perovskite hydrides by DFT calculations. *Int J Hydrogen Energy*. 2023;48(63): 24401–24411.
7. Xu NL, Chen Y, Chen SJ, Zhang WB, Li S, Shi ZF. Electronic structure, mechanical, optical, and thermodynamic characteristics of cubic perovskite $LiMgF_3$ under pressure effect calculated first-principles. *Physica B*. 2023;666: 415064.
8. Xu NL, Chen Y, Chen SJ, Li S, Zhang WB. First-principles investigation for the hydrogen storage properties of $XTiH_3$ (X=K, Rb, Cs) perovskite type hydrides. *Int J Hydrogen Energy*. 2024;50: 114–122.
9. Zhang JY, Chen Y, Chen SJ, Hou J, Song RJ, Shi ZF. Electronic structure, mechanical, optical and thermodynamic properties of cubic perovskite $InBeF_3$ with pressure effects: first-principles calculations. *Results Phys*. 2023;50: 106590.
10. Islam J, Hossain AKMA. Semiconducting to metallic transition with outstanding optoelectronic properties of CsSnCl3 perovskite under pressure. *Sci Rep*. 2020;10: 14391.
11. Khan UA, Khan NU, Abdullah, Alghtani AH, Tirth V, Ahmed SJ, Sajjad M, Algahtani A, Shaheed T, Zaman A. First-principles investigation on the structural, electronic, mechanical and optical properties of silver based perovskite AgXCl3 (X=Ca, Sr). *J Mater Res Technol*. 2022;20: 3296–3305.
12. Ayaz U, Shazia A, Husain M, Rahman N, Bonyah E. Ab initio investigation of structural, electronic, magnetic, elastic, and optical properties of Cs-based chloro-perovskites $CsXCl_3$ (X=Be and Rh). *AIP Adv*. 2021;11(10): 105215.
13. Ephraim Babu K, Murali N, Vijaya Babu K, Taddesse Shibeshi P, Veeraiah V. Structural, elastic, electronic, and optical properties of cubic perovskite $CsCaCl_3$ compound: an ab initio study. *Acta Phys Pol A*. 2014;125: 1179–1185.
14. Das O, Saiduzzaman M, Hossain KM, Shuvo IK, Rahman MM, Ahmad S, Mitro SK. First-principles calculations to investigate pressure-driven electronic phase transition of lead-free halide perovskites $KMCl_3$ (M=Ge, Sn) for superior optoelectronic performance. *Results Phys*. 2023;44: 106212.
15. Zia A, Murtaza G, Ismail K, Khalil RMA, Hussain MI. Ab-initio calculations of the structural, electronic and optical response of $KXCl_3$ (X=Be, Ca and Sr) for optoelectronic applications. *Comput Condens Matter*. 2022;33: e00737.
16. Lu C, Gong W, Li Q, Chen C. Elucidating stress–strain relations of ZrB12 from first-principles studies. *J Phys Chem Lett*. 2020;11(21): 9165–9170.
17. Sun W, Chen B, Li X, Peng F, Hermann A, Lu C. Ternary Na-P-H superconductor under high pressure. *Phys Rev B*. 2023;107(21): 214511.
18. Zhang W, Yang W, Liu Y, Liu Z, Zhang F. Computational exploration and screening of novel Janus MA2Z4 (M=Sc-Zn, Y-Ag, Hf-Au; A=Si, Ge; Z=N, P) monolayers and potential application as a photocatalyst. *Front Phys*. 2022;17: 63509.
19. Molla MR, Saiduzzaman M, Asif TI, Dujana WA, Hossain KM. Electronic phase transition from semiconducting to metallic in cubic halide $CsYbCl_3$ perovskite under hydrostatic pressure. *Physica B*. 2022;630: 413650.
20. Duan Q, Shen J, Zhong X, Lu H, Lu C. Structural phase transition and superconductivity of ytterbium under high pressure. *Phys Rev B*. 2022;105: 214503.
21. Yu JH, Chen SJ, Chen Y, Hou J, Li S, Shi Z. First-principles study of structural, elastic, electronic and optical properties of cubic perovskite $AgXF_3$ (X=Be, Mg, Ca and Sr) compounds. *Mater Today Commun*. 2023;34: 105258.
22. Li S, Wang H, Sun W, Lu C, Peng F. Superconductivity in compressed ternary alkaline boron hydrides. *Phys Rev B*. 2022;105: 224107.

23. Kumar A, Kumar A, Kumar A, Iram N. Ab-initio study of hybrid perovskites $Cs_2AgGaCl_6$ for solar cells applications. *Hybrid Advances*. 2024;6: 100197.
24. Xu NL, Chen Y, Chen SJ, Zhang WB, Li S, Song RJ, Zhang J. First-principles investigations for the hydrogen storage properties of XVH3 (X=Na, K, Rb, Cs) perovskite type hydrides. *J Mater Res Technol.* 2023;26: 4825–4834.
25. Boudiaf K, Bouhemadou A, Al-Douri Y, Khenata R, Bin-Omran S, Guechi N. Electronic and thermoelectric properties of the layered BaFAgCh (Ch=S, Se and Te): first-principles study. *J Alloys Compd.* 2018;759: 32–43.
26. Bouafia H, Hiadsi S, Abidri B, Akriche A, Ghalouci L, Sahli B. Structural, elastic, electronic and thermodynamic properties of $KTaO_3$ and $NaTaO_3$: ab initio investigations. *Comput Mater Sci.* 2013;75: 1–8.
27. Pfrommer BG, Côté M, Louie SG, Cohen ML. Relaxation of crystals with the quasi-Newton method. *J Comput Phys.* 1997;131(1): 233–240.
28. Chung DH, Buessem WR. The Voigt-Reuss-Hill approximation and elastic moduli of polycrystalline MgO, CaF2, β-ZnS, ZnSe, and CdTe. *J Appl Phys.* 1967;38(6): 2535–2540.
29. Fisher ES, Manghnani MH, Kikuta R. Hydrostatic pressure derivatives of the single crystal elastic moduli of Gd, Dy and Er. *J Phys Chem Solids.* 1973;34(4): 687–703.
30. Kaufmann E, Reiss RD. Approximation of the Hill estimator process. *Stat Probab Lett.* 1998;39(4): 347–354.
31. Ullah R, Reshak AH, Ali MA, Khan A, Murtaza G, Al-Anazy M, Althib H, Flemban TH. Pressure-dependent elasto-mechanical stability and thermoelectric properties of $MYbF_3$ (M=Rb, Cs) materials for renewable energy. *Int J Energy Res.* 2021;45: 8711–8723.
32. Kumar V, Tripathy SK. First-principle calculations of the electronic, optical and elastic properties of ZnSiP2 semiconductor. *J Alloys Compd.* 2014;582: 101–1017.
33. Rashid MA, Saiduzzaman M, Biswas A, Hossain KM. First-principles calculations to explore the metallic behavior of semiconducting lead-free halide perovskites RbSnX3 (X=Cl, Br) under pressure. *Eur Phys J Plus.* 2022;137: 649.
34. Song RJ, Chen Y, Chen SJ, Zhang JY, Shi ZF. First-principles investigation of the ultra-wide band gap halides perovskite XBeF3 (X=Na, K) with pressure effects. *Phys Scr.* 2023;98(12): 125907.
35. Gaillac R, Pullumbi P, Coudert FX. ELATE: an open-source online application for analysis and visualization of elastic tensors. *J Phys Condens Matter.* 2016;28(27): 275201.
36. Xu YQ, Wu SY, Zhang LJ, Wu LN, Ding CC. First-principles study of structural, electronic, elastic, and optical properties of cubic $KNbO_3$ and $KTaO_3$ crystals. *Phys Status Solidi B.* 2017;254(5): 1600620.
37. Song RJ, Chen Y, Chen SJ, Zhang JY, Shi ZF. Pressure induced variations from semiconducting to metallic for halide perovskite NaBeCl3 by first-principle calculations. *Mater Today Commun.* 2023;38: 107706.
38. Shahzad A, Ahmadini AAH, Mahmood Q, Flemban TH, Murtaza G, Kattan NA, Iqbal MW, Ghrib T, Laref A. Study of optoelectronic and thermoelectric characteristics of cesium based halides $CsYbX_3$ (X=Br, Cl) for clean energy harvesting. *ECS J Solid State Sci Technol.* 2021;10(1): 015002.
39. Duan X, Zhang H. Introduction: Two-dimensional layered transition metal dichalcogenides. *Chemical Reviews.* 2024;124(19); 10619–10622.
40. Huang SZ, Fang CG, Feng QY, Wang BY, Yang HD, Li B, Xiang X, Zu XT, Deng HX. Pt-modified ZrS_2/HfS_2 monolayer gas-sensing study. *Langmuir.* 2023;39(7): 2719–2728.
41. Koley S. Intercalation in 2H-$TaSe_2$ for modulation of electronic properties and electrochemical energy storage. *Physica B: Condensed Matter.* 2023;668; 415312.
42. Liang J, Li Y, Yin S, Wan C. Recent advances in organic thermoelectric materials. *ACS Applied Materials & Interfaces.* 2023;15(29): 34956–34963.
43. Singh AK. TMDs research with atomic layer deposition (ALD) technique. In: *2D Transition-Metal Dichalcogenides (TMDs): Fundamentals and Application. Materials Horizons: From Nature to Nanomaterials*. Singapore: Springer; 2025. p.635–691.
44. Kennedy BJ, Prodjosantoso AK, Howard CJ. Powder neutron diffraction study of the high temperature phase transitions in $NaTaO_3$. *Journal of Physics: Condensed Matter*. 1999;11(33): 6319–6327.
45. Zachariah S, Ravanan I. Recent advances in chalcogenides for mid-temperature thermoelectric materials. *Journal of Alloys and Compounds*. 2025;1043: 184187.
46. Chen X, Mao SS. Titanium dioxide nanomaterials: synthesis, properties, modifications, and applications. *Chemical Reviews*. 2007;107(7): 2891–2959.
47. Kudo A, Miseki Y. Heterogeneous photocatalyst materials for water splitting. *Chemical Society Reviews*. 2009;38(1): 253–278.
48. Asahi R, Morikawa T, Ohwaki T, Aoki K, Taga Y. Visible-light photocatalysis in nitrogen-doped titanium oxides. *Science*. 2001;293(5528): 269–271.

49. Kashif M, Anjum N. Tuning the electronic and optical properties of the ZrS_2/PtS_2 van der Waals heterostructure by an external electric field and vertical strain. *ACS Omega.* 2022;7(37), 33453–33460.
50. Ye L, Luan L, Guo R, Zhang Y, Wei X, Fan J, Ni L, Liu C, Yang Y, Liu J, Tian Y, Duan L. Optical and tunable electronic properties of doped PtS_2/ZrS_2 van der Waals heterostructure under the effect of strain and electric field. *Materials Science in Semiconductor Processing.* 2023;164: 107615.
51. Ismailzade IG. X-ray study of the phase transitions in $NaTaO_3$. *Kristallografiya.* 1963;8: 363–367. (In Russian)
52. Ma Y, Wang X, Jia Y, Chen X, Han H, Li C. Titanium dioxide-based nanomaterials for photocatalytic fuel generations. *Chemical Reviews*. 2014;114(19): 9987–10043.
53. Khan SUM, Al-Shahry M, Ingler WB. Efficient photochemical water splitting by a chemically modified n-TiO_2. *Science*. 2002;297(5590): 2243–2245.
54. Chen X, Liu L, Yu PY, Mao SS. Increasing solar absorption for photocatalysis with black hydrogenated titanium dioxide nanocrystals. *Science*. 2011;331(6018): 746–750.
55. Li F, Wu H, Cui H. Favorable adsorption and sensing properties of the HfS_2 monolayer upon H_2S and SOF_2 gases by Pt-doping: A first-principles study. *Computational and Theoretical Chemistry*. 2025;1244: 115031.
56. Iram N, Kumar A, Kumar A, Raza A. Ab-Initio Atomistic Analysis of K_2CdSn and Rb_2CdSn Alloys: A Step towards Efficient Photovoltaics, *Discover Electronics*. 2026;3: 55.
57. Kumar A, Gautam R, Chand S, Kumar A, Singh RP. First principle electronic, magnetic and thermodynamic characterization of heavy fermion ternary rare earth metal alloys. *Materials Physics and Mechanics*. 2019;42(1): 112–130.
58. Nguyen QH, Tran KV, Quach SGK, Doan QT, Nguyen NPA, Nguyen TSM, Nguyen DH, Tran AT. Elastic deformation and elastic wave velocity in metals (Au, Cu) and interstitial alloy (CuSi) with FCC structure. *Materials Physics and Mechanics*. 2025;53(3): 165–176.
59. Kumar A, Kumar A, Jain P, Pundir SK, Singh N. TB-mBJ for doping concentration effects on magneto-optical properties in $ZnMnxSn_{(1-x)}As_2$ spintronics materials. *Optik*. 2024;315: 172039.
60. Kumar A, Gupta H, Kumar A, Kumar A, Sharma SK, Lal B, Iram N. Optoelectronic properties of Sb doped GaAs: DFT investigation. To be published in *Indian Journal of Physics*. [Preprint] 2024. Available from: doi.org/10.1007/s12648-024-03273-6.
61. Kumar A, Kumar A, Iram N. First-principles calculations to investigate structural, electronic, mechanical and optical properties of $SrAlO_3$ compound. *Hybrid Advances*. 2024;6: 100211.